From isolation to detection, advancing insights into endothelial matrix-bound vesicles

Sahimy Ayus-Martinez[a,1], **William Meza-Morales**[a,1], **Jesus Jimenez-Osorio**[a], **Maria Buendia-Otero**[a], **Luis López**[b], **Lisandro Cunci**[b], **Donald O. Freytes**[c], **Camilo Mora**[a,*]

[a]Department of Chemical Engineering, University of Puerto Rico-Mayaguez, Route 108, Mayaguez, Puerto Rico, USA

[b]Department of Chemistry, University of Puerto Rico-Rio Piedras, 601 Av. Universidad, San Juan, PR, USA

[c]The Joint Department of Biomedical Engineering, North Carolina State University/University of North Carolina at Chapel Hill, 4130 Engineering Building III, Campus Box 7115, Raleigh, NC, 27695, USA

Abstract

Matrix-bound vesicles (MBVs), an integral part of the extracellular matrix (ECM), are emerging as pivotal factors in ECM-driven molecular signaling. This study is the first to report the isolation of MBVs from porcine arterial endothelial cell basement membranes (A-MBVs) and thyroid cartilage (C-MBVs), the latter serving as a negative control due to its minimal vascular characteristics. Using Transmission Electron Microscopy (TEM), Nano-Tracking Analysis (NTA), Electrochemical Impedance Spectroscopy (EIS), and Atomic Force Microscopy (AFM), we orthogonally characterized the isolated MBVs. We detected the presence and preservation of vascular endothelial cadherin (CD144) in A-MBVs, its low to non-detetcted in C-MBVs, in which SOX9, a chondrocyte marker, was detected. Moreover, we developed a prototype of an immuno-functionalized screen-printed electrode designed for the immunoadsorption of CD144+ MBVs. This device facilitated the electrochemical detection of the targeted vesicles and allowed for their subsequent topological characterization using AFM, which verified the integrity and morphology of CD144+ MBVs post-immunoadsorption. These advancements enhance our comprehension of

*Corresponding author., camilo.mora@upr.edu (C. Mora).
[1]Authors has equal contributions.

Conflicts of interest

There are no conflicts to declare.

CRediT authorship contribution statement

Sahimy Ayus-Martinez: Writing – original draft, Methodology, Investigation, Formal analysis, Data curation. **William Meza-Morales:** Methodology, Investigation, Formal analysis, Data curation, Writing – original draft, Writing – review & editing, Validation. **Jesus Jimenez-Osorio:** Writing – original draft, Formal analysis. **Maria Buendia-Otero:** Investigation. **Luis López:** Validation, Methodology, Formal analysis, Data curation. **Lisandro Cunci:** Validation, Formal analysis, Data curation, Conceptualization. **Donald O. Freytes:** Validation, Methodology, Formal analysis. **Camilo Mora:** Writing – review & editing, Writing – original draft, Visualization, Validation, Supervision, Software, Resources, Project administration, Methodology, Funding acquisition, Formal analysis, Data curation, Conceptualization.

MBVs as conveyors of tissue-specific signals and pioneer new avenues for harnessing their cargo in biomedical applications. This research sets a significant precedent for future studies on the application of MBVs in regenerative medicine and ECM signaling.

Keywords

Matrix-bound vesicles; VE-Cadherin-CD144−; Endothelial extracellular vesicles; Biomarker; Electrochemical detection; Biosensor

1.   Introduction

Extracellular vesicles (EVs) constitute a diverse group of nano-sized structures carrying various biomolecules such as proteins (transmembrane and intraluminal), metabolites, DNA, and miRNA enclosed by lipid bilayers.[1,2] Most types of cells release EVs into the extracellular environment,[3] and their cargoes represent a molecular signaling snapshot of the originating cells' status.[4] Initially considered part of cellular waste management systems,[5,6] EVs influence cell fate responses and reflect cell/tissue status, such as homeostasis, inflammation, and neoplasm.[7–9] Furthermore, recent research has unveiled the role of EVs as valuable biomarkers for monitoring various diseases, including cancer, liver injury, autoimmune diseases, endothelial-EVs in cardiovascular diseases, and other pathologies.[7,8,10–12]

Among EVs, matrix-bound vesicles (MBVs) are EVs embedded in the extracellular matrix (ECM) and distinguished by their tissue-specific features potentially linked to cell regulatory processes.[13] MBVs carry biomolecules (intraluminal and transmembrane) that reflect the ECM of origin, embodying their source tissue's molecular and physiological characteristics.[14–17] These new types of vesicles mimic the specific cell fate responses the ECM directs, making them valuable as EV models in engineering tools for studying ECM molecular signaling.[18–20] Although MBVs hold promise for regenerative medicine, their innovative nature and the insufficient characterization of specific biomarkers present significant challenges for practical integration and translation, as these remain underexplored.[21,22] For this reason, it is crucial to establish standardized workflows that facilitate the identification and biomolecular cargo analysis, enabling more effective utilization in biomedical applications.

The research presented here focuses on Vascular Endothelial Cadherin (CD144), a well-established cell-cell junction biomarker in endothelial tissues.[23,24] CD144 is crucial for maintaining the integrity of the endothelial barrier and is involved in endothelial injury during inflammation; elevated EV levels can signal endothelial dysfunction.[23] Indicating the relevance of CD144 in cardiovascular disease.[10,25] Our research focuses on the premise that MBVs from endothelial cell basement membranes (A-MBVs) will exhibit significantly higher levels of CD144 compared to those from non-endothelial thyroid cartilage tissue (C-MBVs). This study aims to deepen our understanding of MBVs and develop immuno-functionalized tools for their selective adsorption, specifically targeting the CD144+ protein cargo.

To this end, this work comprehends the isolation and comparison of MBVs from artery endothelial cell basement membranes (A-ECM tissue) with those from non-endothelial thyroid cartilage tissue (C-ECM tissue), as illustrated in Fig. 1. The orthogonal characterization of A-MBVs using Transmission Electron Microscopy (TEM), Nano Tracking Analysis (NTA), Electrochemical Impedance Spectroscopy (EIS), and Atomic Force Microscopy (AFM) enhances our understanding of MBVs. It paves the way for further research into their roles in critical pathophysiological processes. For instance, externally added CD144 enhances angiogenesis in hydrogels,[26,27] and tissue-specific EVs could serve as biomarker models for developing detection tools like biosensors.

In this study, we targeted the detection CD144 as a likely protein-cargo in MBVs isolated from arterial endothelial cell-basement membranes (A-MBVs) using immunosorbent assays, with quantification provided by enzyme-linked immunosorbent assay (ELISA). In contrast, CD144 was not detected in MBVs derived from thyroid cartilage (C-MBVs), reflecting the absence of endothelial-associated elements. However, SOX9, a chondrocyte biomarker, was detected in MBVs from C-MBVs. An immunofunctionalized detection device was developed, capable of detecting CD144 in EV samples through electrochemical changes, reducing the required sample volume tenfold compared to traditional ELISA methods. AFM was employed to examine the morphology of CD144+ MBVs and commercial EVs (Fig. 1), confirming successful immunoadsorption and consistency with TEM imaging. This research advances our understanding of MBVs as carriers of ECM signals and sets the stage for further advancements in biomedical research involving MBVs carrying tissue-specific markers. The development of novel characterization tools, such as electrochemical techniques and AFM, helps address the challenges of heterogeneity in the EV field by enhancing the selectivity in characterizing EV populations.

2. Methodology

2.1. Reagents and materials

The following reagents and materials were used: deionized (DI) water with a conductivity of 18.2 MΩcm, 70% ethanol solution, Dulbecco's phosphate buffered saline (DPBS) (Genesee Scientific), 4% sodium deoxycholate (SDC) solution (Millipore-Sigma), deoxyribonuclease (DNase) grade II solution (Millipore-Sigma), collagenase type II (Millipore-Sigma), tris base buffer (pH 8.0, 1 M) (Millipore-Sigma), 0.1% peracetic acid solution, 25 mM trehalose solution (Millipore-Sigma), 5 M sodium chloride (NaCl) solution (Millipore-Sigma), 1 M calcium chloride (CaCl$_2$) solution (Millipore-Sigma), 1 M magnesium chloride (MgCl$_2$) solution (Millipore-Sigma), 0.1 M potassium chloride (KCl) solution (Millipore-Sigma), potassium ferricyanide (K$_3$[Fe(CN)$_6$]) solution (Millipore-Sigma), potassium ferrocyanide (K$_4$[Fe(CN)$_6$]) solution (Millipore-Sigma), 11-mercaptoundecanoic acid (MUA) (Millipore-Sigma), N-(3-dimethylaminopropyl)-N′-ethyl-carbodiimide (EDC) solution (Millipore-Sigma), bovine serum albumin (BSA) (Millipore-Sigma), tris buffered saline (TBS) (Bio-Rad) and tween 20 solution (T) (Bio-Rad). Additional reagents and materials included proteinase K and buffer ATL from Qiagen, rat anti-pig CD144 and goat anti-rat (H/L) (HRP) from BioRad, and rabbit polyclonal to SOX9 and goat anti-rabbit IgG H&L (HRP) from Abcam.

Kits employed included the QuantiFluor dsDNA system from Promega, ExoQuick Ultra from System Biosciences, and ELISA kits for pig CD144 (pCD144) from LS Bio, human CD144 from Abcam, and human SOX9 from RayBiotech. These reagents, materials, and kits were integral for various protein detection and quantification assays. Commercial EVs (exosomes) from pooled human saliva (h.Sal-EVs) (System Biosciences, EXOP-510A-1) were used as EV controls, as EVs from saliva have been reported to carry CD144.

2.2.   ECM decellularization

Preparation of endothelial cell basement membrane from arterial tissue consisted of separating the ascending aorta from the porcine hearts and carefully peeling the arterial tissue. Approximately 7 cm-long sections of the ascending aorta were dissected and opened, as shown in Fig. 1 (open aorta). The basement membrane was then carefully scraped to separate and remove any remaining vascular wall, obtaining a thin sheet of tissue called artery basement membrane (A) by a method similar to urinary bladder matrix (UBM) processing used in clinical applications of ECM biomaterials. This tissue, collected from five arteries, was extensively washed with DPBS and stored at −80 °C for decellularization.

Non-endothelial thyroid cartilage tissue was excised from the trachea of 7–10 pigs. Each larynx was opened to expose the vocal fold area and then sectioned to facilitate cartilage removal, ensuring all connective tissues and muscles were cleared away to prevent contamination from endothelial-related tissue. The cartilage was minced into 3×3 mm cubes, rinsed with deionized water to eliminate residual blood, and stored at −20 °C until decellularization.

Decellularization of arterial and cartilage tissue was performed following the standardized protocol by Mora-Navarro et al. and Biehl et al., with modifications.[20,28]. The procedure began with three 10-min rinses with DI water, 1X DPBS, and again with DI water. This was followed by a 1-h treatment in 4% SDC solution and another 1-h wash in 1 mg/mL DNase grade II solution. Between treatments, tissues were rinsed with DI water, 1X DPBS, and DI water. Final sterilization included an ethanol and peracetic acid solution and three subsequent rinses as previously described (see Table 1 for the summary of all decellularization steps). The effectiveness of decellularization was monitored in real-time through a UV–visible spectrophotometer (see Figure s1), which measured DNA and protein release at 260 nm and 280 nm wavelengths.[29] After washing, the decellularized ECMs (dECMs) were lyophilized overnight and stored at room temperature.

Also, the effectiveness of decellularization was evaluated by quantifying residual double-stranded DNA (dsDNA) in the dECM. ECM in clinical use is reported with less than 2 µg of dsDNA per mg dry ECM.[30–32] Lyophilized samples were ground and digested as follows: for 3 mg of A-ECM, digestion began with an initial 24-h incubation in 800 µL of 0.2 mg/mL collagenase type II in a 50 mM tris base buffer (pH 8.0) containing 0.2 M NaCl, 5 mM $CaCl_2$, and 0.5 mM $MgCl_2$. This was followed by an overnight incubation at 60 °C with 20 µL of 20 mg/mL proteinase K and 180 µL of buffer ATL. For 3 mg of C-ECM, digestion with 20 µL of proteinase K and 180 µL of ATL was sufficient. Digested samples were diluted 1:50 with 1X TE buffer (pH 7.4, Promega) and further diluted two-fold to match the

standard range of the QuantiFluor dsDNA system kit. Quantification was performed using a Spark multimode microplate reader (TECAN) per the manufacturer's instructions.

2.3. MBVs isolation method

dECM was ground into a fine powder and enzymatically digested to release embedded vesicles using a 0.2 mg/mL collagenase type II solution in a buffer containing 0.2 M NaCl, 5 mM $CaCl_2$, and 0.5 mM $MgCl_2$. This solution was added to the dECM to reach a final concentration of 5 mg/mL and incubated at room temperature with constant agitation for 48 h, following a modified protocol from Quijano and Mora.[16,20] Post solubilization, the sample was clarified through centrifuging at 500 g for 10 min, 2,500 g for 20 min, and 10,000 g for 30 min to remove ECM fibers and remaining debris, following the protocol by Mora et al. The resulting samples were filtered using a 0.2 μm filter (Fisher Scientific) followed by ultrafiltration (UF) to concentrate MBVs. An Amicon ultrafiltration tube (Millipore Sigma) of 100 kDa was used. The solution was centrifuged at 4,000 g for 5 min several times. Sample volumes were typically reduced from 15 mL to 500 μL or 20 mL–1 mL. For the purification of MBVs, we employed a commercial affinity-based polymer precipitation technique, as detailed in Ref.33 Specifically, we used the EV-validated ExoQuick Ultra kit (SBI, System Bioscience) to isolate and purify MBVs according to the manufacturer's instructions. Briefly, 67 μL of ExoQuick was added to 250 μL of MBVs sample incubated on ice for 30 min and later centrifugated at 3,000 g for 10 min; the obtained pellet was resuspended in the kit's buffer and later passed through the resin; column was later washed to recover MBVs, achieving a final volume of approximately 500 μL.

2.4. MBV characterization and targeted tissue-specific protein detection

2.4.1. Protein quantification—We determined protein presence using the BCA protein assay kit (Millipore Sigma), with BSA as the standard. Briefly, 25 μL of each sample and standard were reacted with BCA and cupric sulfate solution, and absorbance was read at 562 nm using a Spark multimode microplate reader (TECAN).

2.4.2. Nano-Tracking Analysis (NTA)—MBVs were analyzed using a NanoSight LM100 system (Malvern Panalytical Instruments). Videos were recorded and analyzed using NTA software (version 3.1), with a camera level of 11 and a detection threshold of 3, at a controlled temperature of 20–22 °C. Samples were diluted in 0.22 μm filtered DPBS with 25 mM trehalose at ratios of 1:10, 1.5:10, and 2:10. Particle number and size distribution were determined from an average of three 60-s videos.

2.4.3. Transmission Electron Microscopy (TEM)—Copper carbon formvar 400-mesh grids were glow-discharged prior to sample loading. The grid was floated on a drop of the sample for 10 min, then washed twice by floating on drops of filtered deionized water. Following this, a 2% uranyl acetate solution was applied as a negative stain. Excess stain was blotted with Whatman paper, and the grid was air-dried. Imaging was performed using a JEOL 1230 TEM.

2.4.4. Immunosorbent characterization of MBVs

2.4.4.1. Dot blot analysis.: The presence of CD144 was analyzed in MBVs using a dot blot approach. A 5 μL sample (approx. 1×10^8 particles/mL) was applied to a nitrocellulose membrane (0.22 μm, Bio-Rad), blocked with 1 mL of 5% BSA in TBS-T (Bio-Rad), and incubated with primary antibodies against pCD144 (2.5 μg/mL, Bio-Rad) and SOX9 (2 μg/mL, Abcam) for 90 min. Following primary antibody incubation, membranes were washed with TBS-T and incubated with appropriate HRP-conjugated secondary antibodies. Chemiluminescence detection was performed using a ChemiDoc instrument (Bio-Rad).

2.4.4.2. ELISA.: CD144 and SOX9 levels were quantified using specific ELISA kits. The plates were pre-coated with antibodies against the target proteins. Samples were added and incubated according to the manufacturer's protocols. Following incubation with detection reagents and appropriate washes, colorimetric development was performed using a TMB substrate and stopped with a stop solution. Absorbance was measured at 405 nm.

2.5.   Integrative analysis of CD144+ EVs (MBVs and h-saliva-EVs)

2.5.1.   Electrochemical detection device development—Screen-printed electrodes (SPEs) were obtained from BASi Instruments. Parafilm was used to mask the reference and counter electrodes to functionalize the working electrode area, exposing only the gold (Au) working electrode of 2 mm diameter, as depicted in Fig. S2. This selective exposure was crucial to preserve the integrity of the reference electrode while functionalizing the working electrode. The SPE was then immersed in a 10 mM solution of MUA at 4 °C for 3 h to form a thiol-terminated self-assembled monolayer (SAM) on the gold surface. Subsequently, the electrode was rinsed with DPBS and 70% ethanol to remove unbound MUA. Electrochemical surface changes were monitored using a potentiostat interface 1010E with Gamry DigiElch 8 software (Gamry Instruments). In the next step, the working electrode was incubated for 36 h at 4 °C with a mixture of 5 μM of EDC and anti-CD144 antibody (0.005 mg/mL) to immobilize the antibodies on the surface, enabling selective capture of MBVs carrying pCD144.

2.5.2.   Electrochemical sensing—We utilized a 5 mM equimolar solution of $K_3[Fe(CN)_6]/K_4[Fe(CN)_6]$ in 0.1 M KCl for all electrochemical assessments, performed using the potentiostat interface 1010E (Gamry Instruments) equipped with Gamry DigiElch 8 software. Employing a conventional three-electrode system, we conducted several electrochemical techniques. Cyclic voltammetry (CV) was carried out at varying scan rates (20, 50, 100, 250, and 500 mV/s), starting from an initial voltage of −0.2 mV to a final voltage of 0.5 mV, across three cycles to identify functionalization steps. Electrochemical impedance spectroscopy (EIS) maintained a potential of 0.100 mV and scanned frequencies between 0.1 Hz and 100 kHz, with resistance to charge transfer (Rct) assessed using electrochemical models. In differential pulse voltammetry (DPV), the potential swept from −0.2 V to +0.5 V, employing a step size of 25 mV/s and a pulse size of 50 mV/s. For MBV detection, a 3 μL sample was placed on pAntiCD144 functionalized SPE surfaces for 20 min, followed by washing with DPBS to remove unbound molecules. Detection was quantified using the same electrochemical techniques, allowing evaluation of the capture

efficiency of the MBVs through interactions with specific antibodies on the SPE surfaces, signifying potential applications in targeted biomarker analysis.

2.5.3. Immunoadsorbed MBVs morphology analysis through atomic force microscopy (AFM)—AFM measurements were conducted using an Agilent 5500 atomic force microscope in tapping mode. Each scanned area was 0.425×0.425 µm, captured at a resolution of 512 pixels per line across 512 lines per image, with a scan rate of 1 line per second. Data analysis was performed using the Nanoscope8 software.

2.6. Statistical analysis

Statistical analyses were conducted using GraphPad PRISM version 9.0. Experiments were replicated a minimum of three times, except as noted. dsDNA quantification was analyzed using the Student's unpaired *t*-test. ELISA results were evaluated through a non-linear sigmoidal 4-PL curve fit with 95% confidence intervals. Statistical significance was defined at a p-value of less than 0.05 unless otherwise specified.

3. Results

3.1. Tissue-specific MBV isolation

To evaluate the presence of target proteins in matrix-bound vesicles (MBVs) isolated from tissue-specific extracellular matrices (ECM), we analyzed two tissue groups: endothelial tissues (e.g., endothelial cell-basement membrane) and non-endothelial tissues (e.g., cartilage). Based on previous studies, CD144, an established endothelial cell-junction marker, was chosen as the target protein [34–36]. We expected that MBVs isolated from endothelial tissues would contain endothelial-related markers like CD144, while these markers would likely be absent or undetectable in non-endothelial tissues such as cartilage. Given its avascular nature,[37,38] cartilage was a rational choice for a negative control.

3.2. Tissue decellularization

Fig. 2A presents a macro view of each native tissue sample in the top panel, while the bottom panel displays the macro view of the decellularized (dECM) of the respective tissues. The two different tissues exhibited significant changes in appearance after the decellularization process, transforming into white acellular scaffolds. This transformation was particularly notable in blood-rich tissues such as the artery. The H&E imaging (Fig. 2 A i–iv) shows the remotion of the nuclei (dark purple dots) before and after decellularization.

A standardized decellularization process would enable an adequate comparison across dECM biomolecules, reducing the confounding effects of native cellular components or variations in decellularization reagents.[28,29,39] Approximately 1 g of A-ECM and C-ECM tissues were processed for decellularization, following the protocol outlined in the methodology section (Table 1). SDC was employed as a detergent, and DNase was used to cleave DNA residues within the tissue. Decellularization progress was continuously monitored by automatically sampling aliquots from the bioreactor every 30 s and measuring their absorbance at 260 nm using a UV–visible spectrophotometer, see Fig. S1. This

monitoring allowed track of nucleic acid concentration, including double-stranded DNA (dsDNA), throughout the decellularization process.[29]

Fig. 2B presents a plot of absorbance at 260 nm versus time (hours), revealing distinct peaks corresponding to different decellularization stages. From 0.5 to 1.5 h, tissues underwent the detergent stage with 4% SDC, where absorbance peaked at 0.389 for A-ECM and 0.249 for C-ECM, indicating an increase in nucleic acids. As the process continued, the monitoring curves stabilized, suggesting a saturation of nucleic acids in the bioreactor. A second peak, observed following the addition of DNase (1 mg/mL), showed absorbance levels reaching 0.529 for A-ECM and 0.543 for C-ECM. These results highlight differences in absorbance between tissue types and confirm the method's effectiveness in correlating absorbance with nucleic acid concentrations, emphasizing successful intracellular content removal, which is critical for refining ECM.

The residual dsDNA was quantified in the acellular dECM, following standard procedures. Fig. 2C illustrates the reduction in dsDNA levels for both A-dECM and C-dECM, comparing the amounts in native tissues (dark grey bars) with those in decellularized dECM (light grey bars). The dsDNA quantification assays were performed in triplicate for each tissue type. Statistical analyses using GraphPad Prism software and an unpaired Student's *t*-test revealed significant differences ($P < 0.05$) between native and dECM tissues. Notably, the reduction in μg of dsDNA per mg of dry tissue was substantial: from 2.276 ± 0.735 to 0.191 ± 0.246 μg/mg for A-ECM, and from 0.682 ± 0.263 to 0.074 ± 0.059 μg/mg for C-ECM.[40] Despite the initially low dsDNA content in C-ECM, the reduction remained significant, underscoring the efficacy of the decellularization protocol.

This significant reduction in DNA content is crucial for biomaterial applications, as residual nucleic acids can provoke immune responses. Post-decellularization, the acellular scaffolds were lyophilized at −80 °C and 0.15 mbar, preparing them for subsequent MBV isolation, which involved further ECM processing to release the embedded MBVs.

3.3. Morphology and size characterization of isolated MBVs

MBVs released from the dECM were characterized for size and morphology using NTA and TEM, as depicted in Fig. 3. A 50 μL aliquot of Cartilage derived MBVs and Artery derived MBVs were diluted 12-fold and 10-fold, respectively, using 1X DPBS to measure particle size distribution and concentration. Fig. 3A and B illustrate representative particle size distributions for A-MBVs and C-MBVs, respectively, selected from several analyzed batches. The NTA results showed that C-MBVs exhibited a higher particle concentration, with an average of $1.26 \times 10^{10} \pm 5.52 \times 10^8$ particles/mL. In comparison, A-MBVs had a lower concentration at $8.46 \times 10^9 \pm 1.30 \times 10^8$ particles/mL. Additionally, C-MBVs had larger average particle sizes, measuring 297.9 ± 6.3 nm compared to 251.5 ± 23.2 nm for A-MBVs. These averages were derived from measurements recorded by the instrument, and the figures represent the particle size distribution of the sampled populations. These findings suggest that MBVs from cartilage-derived dECM are both more abundant and more significant, reflecting possible differences in the structural or functional attributes of the dECM between the two tissue types (see Fig. S3).

Fig. 3C and D shows TEM images of isolated MBVs, with red arrows pointing to the vesicles. NTA and TEM analyses aligned with detecting particles below the 200 nm range. Both techniques also showed evidence of EV aggregation, which appears to be enlarged in the images. Fig. 3D and Fig. S3 illustrate various MBVs aggregated on the left side, resulting in an approximate size of 350 nm. This observation is consistent with classical observations of extracellular vesicles.[16,41] The TEM images show that MBVs possess a rounded morphology and a bilayer membrane structure characteristic of such vesicles (enlargements of Fig. 3C and D). This uniformity in shape across samples indicates a successful isolation process, confirming the integrity of the MBVs extracted. The clear visualization of these vesicles supports their identification and highlights the potential for their utilization in further biomolecular analyses.

3.4. Immunosorbent characterization of isolated MBVs

The presence of CD144 in the MBVs was evaluated using immunosorbent assays (Dot Blot).[42,43] A-MBVs, originating from endothelial-rich tissues, were expected to contain the tissue-specific biomarker CD144. Conversely, C-MBVs were anticipated to carry SOX9, associated with chondrocytes, and little to no CD144. Commercial extracellular vesicles isolated from human saliva (h.Sal-EVs) (System Bioscience, SBI, CA, USA) served as a positive control due to the established presence of CD144 in circulating EVs.[36,44]

Fig. 4A and B presents Dot Bot analyses with 3 μL samples of h.Sal-EVs, A-MBVs, and C-MBVs, each at a concentration of 1 μg/mL of total protein. Fig. 4A shows the detection of CD144 in h.Sal-EVs and A-MBVs, with no detectable CD144 in C-MBVs. A separate blot was conducted to detect SOX9 in the same samples, as shown in Fig. 4B, revealing the presence of SOX9 in h.Sal-EVs, A-MBVs, and C-MBVs. The distinct patterns observed in the dot blot analysis suggest specific expression profiles of CD144 and SOX9 across different MBV sources, suggesting their potential roles in cellular communication.

Following confirming CD144 presence, biomarkers were quantified using ELISA as a validated immunoassay and benchmark control. The ELISA results are presented in Fig. 4C and D. For CD144, concentrations were measured as 1.429 ± 0.391 ng/mL in h.Sal-EVs and 0.517 ± 0.032 ng/mL in A-MBVs, as shown in Fig. 4C. CD144 was undetectable in several assays for C-MBVs. The ELISA kit used for CD144 (Abcam), had a minimum detection threshold of 0.331 ng/mL. Data was fitted using a non-linear model ($R^2 = 0.9980$), with a linear curve fit provided in Supplemental Fig. S4.

Fig. 4D details the ELISA results for SOX9, showing concentrations of 2.169 ± 0.165 ng/mL in h.Sal-EVs, 0.929 ± 0.152 ng/mL in A-MBVs, and 1.064 ± 0.174 ng/mL in C-MBVs. SOX9 was detected in all samples analyzed. The ELISA kit for SOX9 (RayBiotech), features a minimum detection limit of 0.41 ng/mL. Results were estimated using a non-linear fit ($R^2 = 0.9842$), and a linear curve fit is available in Supplemental Fig. S5.

3.5. Characterization of the electrode functionalization

Following the characterization of A-MBVs, electrochemical analysis was employed for the detection of the CD144 biomarker within the A-MBVs. This approach is supported by previous studies that have indicated that altering the surface of the electrodes enhances the

detection signals of biomarkers.[45] Our study uses antibodies, which enhance the detection of the target molecule and reduce non-specific adsorption on the electrode surface.[46] Thus, the electrochemical properties of the surface were analyzed both before and after its modifications. Gold electrodes were studied to understand the changes produced by the immobilization of the antibody, Anti-CD144, on the electrochemistry of the surface. A solution of 5 mM of $K_3Fe(CN)_6$/$K_4Fe(CN)_6$ with 0.1 M KCl was used to characterize the modified electrode surface.

Fig. 5A and B illustrate cyclic voltammetry (CV) analyses conducted at a scan rate of 100 mV/s on modified gold electrodes. Fig. 5A shows the results for human saliva-derived extracellular vesicles (h.Sal-EVs, control), while Fig. 5B depicts the results for artery-derived MBVs (A-MBVs). The electrode modifications included: the baseline gold surface (Au), the surface after modification with MUA (Au/MUA), and the final stage following antibody immobilization targeting the CD144 protein (Au/MUA/Anti-CD144).

In Fig. 5A and B, the CV plots show changes in the kinetics of the redox reaction. These changes are observed in the change of the peak-to-peak potential between the oxidation and reduction peaks. Also, a decrease in electrical currents and a reduction in reaction reversibility were observed due to Anti-CD144 immobilization, as indicated by the increased separation between the oxidation and reduction peaks. The oxidation and reduction peak currents at different scanning rates were plotted against the square root of the scan rates ($v^{1/2}$) in Fig. 5C. Peak currents not only decreased but also deviated from linearity with respect to $v^{1/2}$, particularly in the case of Anti-CD144, meaning that the redox reaction is not limited by electron transfer kinetics due to the blocking effect of the antibodies.

Electrochemical impedance spectroscopy (EIS) was utilized to investigate the chemical modifications on the surface of Anti-CD144-modified electrodes. The EIS data revealed increased charge transfer resistance (Rct) following the immobilization of Anti-CD144, indicating a more resistive surface due to the antibody layer. This increase in Rct is consistent with the expected blocking effect of the antibody, which hinders electron transfer at the electrode interface. Fig. 6A and B illustrate these changes, highlighting the elevated Rct values observed after Anti-CD144 functionalization.

Fig. 6 shows the EIS of **A**. Au Bare, Au/MUA, AU/MUA/anti-CD144, and Au/MUA/anti-CD144/h.Sal-EVs. **B.** Au Bare, Au/MUA, AU/MUA/anti-CD144 and Au/MUA/anti-CD144/A-MVBs. EIS is a robust analytical method for detecting changes in electrode interfacial properties and analyzing the interactions between analytes and their immobilized probing molecules on electrode surfaces.[47] Differences in antibody immobilization affect mass transport limitations, an expected outcome due to the higher charge transfer involved. Fig. 6C shows the circuit used to model the EIS of the modified gold electrodes, which was chosen because of the use of the redox couple $K_3[Fe(CN)_6]$/$K_4[Fe(CN)_6]$.[48]

Fig. 6A depicts the Nyquist plot of the different functionalization steps and attached is h.Sal-EVs, the small black semicircle represents a typical response from the electrode without modifications with an Rct, 0.383 kΩ; this semicircle increases significantly after MUA functionalization (Rct=19.589 kΩ, red semicircle), and later decreases with the

immobilization of the antibody (Rct=2.556 kΩ, green semicircle), finally once the h.Sal-EVs were incubated in the working electrode, and an Rct of 4.761 kΩ was measured (blue semicircle), meaning a decrease in electron transfer due to vesicle binding to the antibodies on the gold electrode surface.

Similar behavior was observed for the impedimetric detection of A-MBVs (Fig. 6B). Rct of the gold electrode without modification was 0.890 kΩ (black semicircle), functionalization of MUA increased the Rct to 10.490 kΩ (red semicircle), immobilization of antibody significantly decreased the Rct to 1.768 kΩ (green semicircle) showing an increase in electron transfer through the antibody, and A-MBVs were detected by EIS again as a decrease in electron transfer due to vesicle binding to the antibody observed as a decrease in Rct, going to 3.061 kΩ (purple semicircle), showing a successful attachment of A-MBVs to the immunosensor and electrochemical detection through impedimetric assay.

Fig. 6D and E depict the changes in Rct due to adding h.Sal-EVs and A-MBVs across different experiments (n = 3). The best-performing electrodes are displayed. The results of Rct were 2.508 ± 0.053 kΩ and 4.700 ± 0.068 kΩ for pAntiCD144 and h.Sal-EVs, respectively, and 1.753 ± 0.017 kΩ and 3.067 ± 0.023 kΩ for pAntiCD144 and A-MBVs. These results indicate the surface modification caused by adding the respective EVs.

3.6. Electrochemical detection of CD144+ EVs

EIS is widely regarded for its high sensitivity in the biorecognition of analytes, such as proteins and enzymes, due to its capability to detect minimal changes in interfacial properties on modified electrodes.[49–51] This technique is particularly advantageous in this study, as it allows for precise monitoring of antibody binding to tissue-specific proteins present in the isolated MBVs. Additionally, EIS requires only a minimal sample volume (<5 μL), making it a suitable method for detecting EVs, where isolation yields are often limited. The changes on the modified working electrode are directly related to the presence of the specific analytes, h.Sal-EVs (EV control) and A-MBVs.

Fig. 6D, blue column, shows the targeting of CD144+ EVs, using h. Sal-EVs with a 0.7 ng/mL concentration of CD144 as a positive control, CD144 concentration was determinate with ELISA, a 3 mL drop was incubated within the working electrode for 20 min, Rct values and other impedance parameters were fitted for the spectra. The Rct was calculated as the difference between the raw Rct response of the incubated h. Sal-EVs and the raw Rct response of the immobilized pAnti-CD144.

Another concentration of CD144 per mL was also used to evaluate the electrochemical behavior; the calculated Rct for the two concentrations 0.233 and 0.712 ng of CD144/mL were plotted in Supplemental Fig. S6. The biosensor was able to detect both concentrations of CD144 in the h.Sal-EVs, for the concentration of 0.233 ng of CD144/mL, the Rct was 0.7817 ± 0.1819 kΩ, and for 0.712 ng of CD144/mL, the Rct was 1.807 ± 0.3462 kΩ for three different experiments.

The Rct of Anti-CD144 and A-MBVs was plotted in Fig. 6E purple column. The difference between AntiCD144 Rct and A-MBVs Rct (Rct) was plotted in Supplemental Fig. S7. This

change was 0.7833 ± 0.0633 kΩ at a concentration of 0.517 ng/mL of CD144 and 469.6 ng of total protein. These results highlight the potential of the developed biosensor for detecting targeted specific markers in EVs.

3.7. AFM validation of CD144+ EV capture on functionalized SPEs

In the context of EV heterogeneity, orthogonal methodologies are crucial for further EV characterization. Using tapping-mode AFM, this section verifies the attachment and morphology of EVs that were immune-adsorbed through CD144 on the functionalized SPE surfaces.

This high-resolution technique not only reinforced the specificity of our electrochemical detection but also confirmed the targeted capture of EVs-like particles, thereby enhancing the reliability of our subsequent analyses.

Fig. 7 presents AFM images of the EVs (h. Sal-EVs and A-MBVs) deposited onto the gold screen-printed electrode surface. The screen-printed electrodes functionalized with pAntiCD144 successfully captured h.Sal-EVs and A-MBVs through the interaction of the endothelial biomarker CD144 within the EVs to the immobilized antibody.

This characterization confirms the biosensor's suitability for detecting EVs carrying the targeted markers. AFM analysis provided insights into the topography and height of these MBVs. Topography images revealed the diameter of isolated MBVs, while height images showed an average height of 20 nm—consistent with values reported by Sharma et al.[52]

Furthermore, the analysis performed using AFM tapping mode provided detailed insights into the physical characteristics of h.Sal-EVs and A-MBVs.

As depicted in Fig. 7A–h.Sal-EVs exhibited a broader size range, with diameters varying from 100 nm to 150 nm. Their shapes were less uniform, potentially reflecting the diverse cellular origins and physiological conditions under which these EVs were produced. In contrast, A-MBVs, shown in Fig. 7C, measured approximately 162 nm in diameter and maintained a visible bilayer structure under high-resolution AFM, indicative of their intact vesicular nature.

The height analysis from AFM of A-MBVs, illustrated in Fig. 7D, further supported these findings. A-MBVs typically exhibited a narrower height distribution around 21.0 nm. Meanwhile, h.Sal-EVs displayed more significant height variations, ranging from 17.5 nm to 24.7 nm, as shown in Fig. 7B. These AFM observations align with TEM analyses performed for the A-MBVs, confirming the robustness of the results and the efficacy of using both AFM and TEM jointly to explore the detailed structural properties of EVs from different sources.

4.   Discussion

Our study evaluates matrix-bound vesicles (MBVs) isolated from two distinct tissues—artery endothelial cell basement membrane (A-tissue) and thyroid cartilage (C-tissue)—to establish an approach for analyzing these complex ECM signaling components.

By employing a standardized decellularization protocol, we seek minimal variability and enhanced reproducibility[28,29,39] in ECM derivation, which is essential for consistently studying their associated biomacromolecules such as endothelial MBVs (A-MBVs). Also, we are developing tailored sensing tools that target biomarkers carried by extracellular vesicles, such as CD144, a transmembrane endothelial marker, for a thorough endothelial-EV characterization.[34,35,53,54]

The ECM derivation system is equipped with an inline UV spectroscopy system (refer to Fig. S1) that enables real-time monitoring of nucleic acid removal from tissues. This monitoring tool represents a significant advancement over previous prototypes reported in the literature for dECM production.[29] The reported decellularization streamlines the process into a three-step washing sequence, comprising 1 h each of contact with SDC detergent and DNase I, completing the process in 6 h. This is an efficiency enhancement compared to traditional methods reported in the literature, which can take 72 h up to 480 h.[40,55,56]

During the decellularization process, the system demonstrated, via inline real-time monitoring, significant increases in nucleic acid levels in the bioreactor's liquid phase during SDC and DNase treatments of both A-tissue and C-tissue. This was evidenced by pronounced nucleic acid concentration peaks, indicative of effective decellularization (see Fig. 2B). The effect was especially prominent in artery samples (A-dECM), where the cellular composition likely contributed to the increased nucleic acid levels. Post-decellularization analysis revealed a marked reduction in dsDNA content across all dECM samples, consistent with H&E staining results. Notably, DNA content in artery dECM decreased by 94%, as depicted in Fig. 2C, corroborating findings from Inal et al.[56] and similar detergent-based decellularization studies.[57,58] For cartilage, dsDNA reduction was approximately 89%, resulting in 74 ng of dsDNA per mg of dry dECM, comparable to findings by Hong[59] (53.21 ng/mg) and Guimaraes[60] (20 ng/mg) dsDNA per mg of dry dECM. All our ECM materials maintained a final dsDNA content below that of the reference urinary bladder membrane ECM (UBM-ECM), already used in clinical applications.[14,21,61]

Characterizing isolated MBVs in terms of size, morphology, and targeted biomolecular proteins offers critical insights into their structure and origin 2. TEM revealed that these vesicles typically exhibit a round shape with a distinctive border, indicative of the characteristic lipid bilayer of extracellular vesicles.[14] Specifically, TEM analysis showed that A-MBVs generally ranged between 200 and 250 nm (Fig. 3A and C), closely aligning with findings from isolated MBVs in the bovine pericardium, which averaged 142 nm.[41] Moreover, C-MBVs displayed a peak size distribution at 200 nm, with TEM images (Fig. 3D) demonstrating spherical forms between 200 and 250 nm, consistent with Shapiro's findings on chondrocyte-derived matrix vesicles.[62]

These dimensions and morphologies are within the typical MBV size range of 50–400 nm reported in the literature.[13,16] In addition, aggregates of MBVs were found, as shown in Fig. 3D; these EV aggregations can occur due to vesicle crowding and complex interactions in biological environments, which may include non-vesicular components acting as adhesive "glue" between vesicles.[63–65] The integrity of MBVs provides strong evidence that the

purification methods were adequate in dissociating the ECM while releasing the EVs into the liquid phase environment.

The immunosorbent characterization of MBVs (i.e., A-MBVs and C-MBVs) regarding the presence or no detection of endothelial-related biomarkers (i.e., CD144) further supports our hypothesis about MBVs carrying tissue-specific proteins. CD144, also known as VE-cadherin, is critical for cell-junction formation, vascular organization, and endothelial assembly, playing a pivotal role in developing the aorta and heart valves.[66] The presence of VE-cadherin in MBVs isolated from A-ECM highlights their potential as carriers of tissue-specific markers, supporting reports posited by other researchers.[12,21,45]

Our findings support that MBVs carry markers associated with their tissue of origin, with endothelial-derived MBVs (A-MBVs) specifically carrying endothelial markers like CD144. This finding is highly relevant for monitoring endothelial-related EVs in diagnosing and understanding cardiovascular diseases such as myocardial infarction and familial hypercholesterolemia.[34] Conversely, the absence of CD144 in MBVs from cartilage tissue, which does not produce the CD144 protein, suggests a specificity of the vesicles' protein content. This finding prompted us to detect SOX9 as a potential cargo in C-MBVs, which was positive in the immunodetection, aligning with SOX9's crucial role in cartilage development and maintenance.[67,68] Additionally, SOX9 presence in A-MBVs might be explained by its involvement in tissue differentiation during embryonic development.[67,69] The detection of SOX9 in MBVs highlights the need for further investigation, mainly focusing on defining tissue-specific protein cargos.[16]

Our research aims to bridge a significant gap in studying transmembrane protein cargos within EVs. We are developing an innovative electrochemical device designed to enhance the detection of EVs, specifically those carrying markers like CD144+ indicative of endothelial cells. Applying electrochemical techniques to MBVs highlights our approach's innovative potential to propel the field of MBV studies.

Fig. 5A and B illustrate significant voltammogram shifts following MUA functionalization, indicating successful antibody immobilization on the SAM. This layer acts as a barrier, impeding electron transfer and enhancing electron flow upon immobilizing pAnti-CD144, which targets the immunoadsorption of CD144+ MBVs.[49] The addition of h.Sal-EVs and A-MBVs on the pAnti-CD144 functionalized working electrode reduced oxidation peaks, suggesting interference in electron transfer at the electrode/electrolyte interface, a behavior consistent with other studies involving mercaptohexanoic acid functionalized SPEs.[70] Electrochemical assays, shown in Fig. 6A and B, demonstrated that MUA significantly increases charge transfer resistance (Rct). Subsequent antibody immobilization reduced this resistance, facilitating interactions between the electrode surface and the ferrocyanide solution. The increase in resistance with the introduction of CD144+ A-MBVs confirms their capacity to obstruct electron transfer, aligning with findings from pathogen and protein detection studies.[51]

The biosensing device developed enhances the characterization of tissue-specific protein targets within MBVs, providing new insights into these underexplored EVs. Preliminary

data indicate that A-MBVs retain detectable biomarkers from their origin tissue. While electrochemical methods have not previously been applied to MBVs, similar strategies have effectively identified exosomes using aptamers or antibodies.[71,72]

Arguably, the immunefunctionalized electrode platform's simple assembly offers a tool to detect biomarkers with just 3 μL of sample volume (15X less sample than an ELISA), underscoring its practical benefits and future translational potential. Given that MBVs are isolated through a complex enzymatic treatment of dECM, orthogonal assays are essential to confirm the lipidic nature of vesicles adsorbed on the biosensing prototype. As illustrated in Fig. 7, AFM imaging successfully validated MBV attachment, with topography images (**A** and **C**) displaying h.Sal-EVs and A-MBVs, respectively, adhered to the functionalized gold screen-printed electrode. Specifically, A-MBVs were shown to bind effectively to the Anti-CD144 functionalized electrode, with images revealing vesicles of varying diameters, thereby confirming targeted capture and characterization.

Fig. 7A illustrates that the diameter of h.Sal-EVs (EV control) is approximately 100 nm, a size consistent with observations in Fig. 7C for A-MBVs. Additionally, Fig. 7D presents a height analysis of the isolated/immune-adsorbed MBVs, revealing a typical height of around 21 nm and the characteristic lipid bilayer previously identified in MBVs.[13,14] A similar height of 24.7 nm is reported in Fig. 7B, which is aligned with findings by Sebaihi[73] on EVs derived from human body fluids.

In our approach, a functionalized SPE equipped with antibodies successfully immunoadsorbs the transmembrane protein CD144 from isolated A-MBVs, showcasing the platform's capability for precise vesicle capture and comprehensive biomolecular analysis. This technique verifies that isolated EVs from the dECM contain tissue-specific biomarkers, suggesting their potential use as culture media supplements to enhance stem cell differentiation. Additionally, the device demonstrates promise for disease prognosis and early detection due to its high sensitivity to low concentrations of these biomarkers.

5. Conclusions

In this study, we successfully isolated MBVs from endothelial cell basement membrane-derived extracellular matrix (A-dECM) and thyroid cartilage-derived ECM (C-dECM). These EVs exhibited the characteristic round morphology and intact membrane structures, as verified by TEM and AFM. The enzymatic digestion protocol effectively preserved the endothelial-specific CD144 marker within the MBVs, confirmed through immunosorbent assays. This data underscores the potential of A-MBVs as carriers of endothelial-related proteins for regenerative medicine and as models for advancing EV-based detection technologies.

Leveraging A-MBVs, we developed a label-free biosensing device that demonstrates significant potential for integration into advanced sensing technologies, offering rapid and scalable detection suitable for both clinical and research applications. Future research will focus on refining the selectivity and specificity of the biosensing device to enhance

performance and facilitate clinical translation while also addressing EV heterogeneity, a current challenge in the field.

During the preparation of this work, the author(s) used [ChatGPT 4.0 and Grammarly] in order to improve readability. After using this tool/service, the author(s) reviewed and edited the content as needed and take(s) full responsibility for the content of the publication.

Supplementary Material

Refer to Web version on PubMed Central for supplementary material.

Acknowledgments

References

1. Piening LM, Wachs RA. Matrix Bound Nanovesicles: what are they and what do they do? Cells Tissues Organs. 2022. 10.1159/000522575.

2. Welsh JA, Goberdhan DCI, O'Driscoll L, et al. Minimal information for studies of extracellular vesicles (MISEV2023): from basic to advanced approaches. J Extracell Vesicles. 2024;13, e12404. 10.1002/jev2.12404. [PubMed: 38326288]

3. Rackov G, Garcia-Romero N, Esteban-Rubio S, Carrión-Navarro J, Belda-Iniesta C, Ayuso-Sacido A. Vesicle-Mediated control of cell function: the role of extracellular matrix and microenvironment. Front Physiol. 2018;9:651. 10.3389/fphys.2018.00651. [PubMed: 29922170]

4. Bonner SE, Willms E. Intercellular communication through extracellular vesicles in cancer and evolutionary biology. Prog Biophys Mol Biol. 2021;165:80–87. 10.1016/j.pbiomolbio.2021.08.006. [PubMed: 34391800]

5. Couch Y, Buzàs EI, Vizio DD, et al. A brief history of nearly EV-erything – the rise and rise of extracellular vesicles. J Extracell Vesicles. 2021;10, e12144. 10.1002/jev2.12144. [PubMed: 34919343]

6. Théry C, Witwer KW, Aikawa E, et al. Minimal information for studies of extracellular vesicles 2018 (MISEV2018): a position statement of the International Society for Extracellular Vesicles and update of the MISEV2014 guidelines. J Extracell Vesicles. 2018;8, 1535750. 10.1080/20013078.2018.1535750.

7. Cho Y-E, Im E-J, Moon P-G, Mezey E, Song B-J, Baek M-C. Increased liver-specific proteins in circulating extracellular vesicles as potential biomarkers for drug- and alcohol-induced liver injury. PLoS One. 2017;12, e0172463. 10.1371/journal.pone.0172463. [PubMed: 28225807]

8. Aqrawi LA, Galtung HK, Guerreiro EM, et al. Proteomic and histopathological characterisation of sicca subjects and primary Sjögren's syndrome patients reveals promising tear, saliva and extracellular vesicle disease biomarkers. Arthritis Res Ther. 2019;21:181. 10.1186/s13075-019-1961-4. [PubMed: 31366407]

9. Nieuwland R, Siljander PR-M, Falcón-Pérez JM, Witwer KW. Reproducibility of extracellular vesicle research. Eur J Cell Biol. 2022;101, 151226. 10.1016/j.ejcb.2022.151226. [PubMed: 35460959]

10. de Freitas RCC, Hirata RDC, Hirata MH, Aikawa E. Circulating extracellular vesicles as biomarkers and drug delivery vehicles in cardiovascular diseases. Biomol. 2021;11:388. 10.3390/biom11030388.

11. Charla E, Mercer J, Maffia P, Nicklin SA. Extracellular vesicle signalling in atherosclerosis. Cell Signal. 2020;75, 109751. 10.1016/j.cellsig.2020.109751. [PubMed: 32860954]

12. Rodrigues-Junior DM, Tsirigoti C, Lim SK, Heldin C-H, Moustakas A. Extracellular vesicles and transforming growth factor β signaling in cancer. Front Cell Dev Biol. 2022;10, 849938. 10.3389/fcell.2022.849938. [PubMed: 35493080]

13. Turner NJ, Quijano LM, Hussey GS, Jiang P, Badylak SF. Matrix bound nanovesicles have tissue specific characteristics that suggest a regulatory role. Tissue Eng. 2022;0. 10.1089/ten.tea.2022.0091.

14. Huleihel L, Hussey GS, Naranjo JD, et al. Matrix-bound nanovesicles within ECM bioscaffolds. Sci Adv. 2016;2, e1600502. 10.1126/sciadv.1600502. [PubMed: 27386584]

15. Hussey GS, Dziki JL, Badylak SF. Extracellular matrix-based materials for regenerative medicine. Nat Rev Mater. 2018;3:159–173. 10.1038/s41578-018-0023-x.

16. Quijano LM, Naranjo JD, El-Mossier SO, et al. Matrix-bound nanovesicles: the effects of isolation method upon yield, purity, and function. Tissue Eng C Methods. 2020;26:528–540. 10.1089/ten.tec.2020.0243.

17. Smirnova O, Efremov Y, Klyucherev T, et al. Direct and cell-mediated EV-ECM interplay. Acta Biomater. 2024. 10.1016/j.actbio.2024.07.029.

18. Hussey GS, Molina CP, Cramer MC, et al. Lipidomics and RNA sequencing reveal a novel subpopulation of nanovesicle within extracellular matrix biomaterials. Sci Adv. 2020;6, eaay4361. 10.1126/sciadv.aay4361. [PubMed: 32219161]

19. Hussey GS, Dziki JL, Lee YC, et al. Matrix bound nanovesicle-associated IL-33 activates a pro-remodeling macrophage phenotype via a non-canonical, ST2-independent pathway. J Immunol Regen Medicine. 2019;3:26–35. 10.1016/j.regen.2019.01.001.

20. Mora-Navarro C, Badileanu A, Martins AMG, et al. Porcine vocal fold lamina propria-derived biomaterials modulate TGF-β1-mediated fibroblast activation in vitro. ACS Biomater Sci Eng. 2020;6:1690–1703. 10.1021/acsbiomaterials.9b01837. [PubMed: 33455360]

21. Huleihel L, Bartolacci JG, Dziki JL, et al. Matrix-Bound nanovesicles recapitulate extracellular matrix effects on macrophage phenotype. Tissue Eng. 2017;23:1283–1294. 10.1089/ten.tea.2017.0102.

22. Crum RJ, Capella-Monsonís H, Chang J, et al. Biocompatibility and biodistribution of matrix-bound nanovesicles in vitro and in vivo. Acta Biomater. 2023;155: 113–122. 10.1016/j.actbio.2022.11.026. [PubMed: 36423817]

23. Žekasa V, Matuzevi ienea R, Kar iauskaitea D, Vitkusa D, Radzevi iusa M, Janiulionieneb A, Linkevi i t a A, Kutkien c S, Ku inskien Z, Changes in circulating endothelial microvesicles in men after myocardial infarction. Adv Med Sci, 65(1), 120–126 | 10.1016/j.advms.2019.12.002, Advms (n.d.) 120–126.

24. Desideri E, Ciccarone F, Ciriolo MR, Fratantonio D. Extracellular vesicles in endothelial cells: from mediators of cell-to-cell communication to cargo delivery tools. Free Radic Biol Med. 2021;172:508–520. 10.1016/j.freeradbiomed.2021.06.030. [PubMed: 34214634]

25. Favero G, Paganelli C, Buffoli B, Rodella LF, Rezzani R. Endothelium and its alterations in cardiovascular diseases: life style intervention. BioMed Res Int. 2014;2014, 801896. 10.1155/2014/801896. [PubMed: 24719887]

26. Gao C, Zhang Y, Xie J, et al. VE-cadherin functionalized injectable PAMAM/HA hydrogel promotes endothelial differentiation of hMSCs and vascularization. Appl Mater Today. 2020;20, 100690. 10.1016/j.apmt.2020.100690.

27. Shuai Q, Cao L, Qin Z, Zhang Y, Gu Z, Yang J. VE-cadherin fusion protein substrate enhanced the vasculogenic mimicry capability of hepatocellular carcinoma cells. J Mater Chem B. 2020;8:1699–1712. 10.1039/c9tb02790d. [PubMed: 32016269]

28. Biehl A, Martins AMG, Davis ZG, et al. Towards a standardized multi-tissue decellularization protocol for the derivation of extracellular matrix materials. Biomater Sci-Uk. 2022;11:641–654. 10.1039/d2bm01012g.

29. Mora-Navarro C, Garcia ME, Sarker P, et al. Monitoring decellularization via absorbance spectroscopy during the derivation of extracellular matrix scaffolds. Biomed Mater. 2022;17, 015008. 10.1088/1748-605x/ac361f.

30. Keane TJ, Londono R, Turner NJ, Badylak SF. Consequences of ineffective decellularization of biologic scaffolds on the host response. Biomaterials. 2012;33:1771–1781. 10.1016/j.biomaterials.2011.10.054. [PubMed: 22137126]

31. Londono R, Dziki JL, Haljasmaa E, Turner NJ, Leifer CA, Badylak SF. The effect of cell debris within biologic scaffolds upon the macrophage response. J Biomed Mater Res, Part A. 2017;105:2109–2118. 10.1002/jbm.a.36055.

32. Cramer MC, Badylak SF. Extracellular matrix-based biomaterials and their influence upon cell behavior. Ann Biomed Eng. 2020;48:2132–2153. 10.1007/s10439-019-02408-9. [PubMed: 31741227]

33. Chugh PE, Sin S-H, Ozgur S, et al. Systemically circulating viral and tumor-derived MicroRNAs in KSHV-associated malignancies. PLoS Pathog. 2013;9, e1003484. 10.1371/journal.ppat.1003484. [PubMed: 23874201]

34. Nielsen MH, Bæk R, Jorgensen MM, Mellergaard M, Handberg A. Increased extracellular vesicles (EVs) related to T cell-mediated inflammation and vascular function in familial hypercholesterolemia. Atheroscler. Plus. 2023;53:16–25. 10.1016/j.athplu.2023.06.004. [PubMed: 37637934]

35. Koga H, Sugiyama S, Kugiyama K, et al. Elevated levels of VE-cadherin-positive endothelial microparticles in patients with type 2 diabetes mellitus and coronary artery disease. J Am Coll Cardiol. 2005;45:1622–1630. 10.1016/j.jacc.2005.02.047. [PubMed: 15893178]

36. Davidson SM, Boulanger CM, Aikawa E, et al. Methods for the identification and characterization of extracellular vesicles in cardiovascular studies: from exosomes to microvesicles. Cardiovasc Res. 2022;119:45–63. 10.1093/cvr/cvac031.

37. Benders KEM, van Weeren PR, Badylak SF, Saris DBF, Dhert WJA, Malda J. Extracellular matrix scaffolds for cartilage and bone regeneration. Trends Biotechnol. 2013;31:169–176. 10.1016/j.tibtech.2012.12.004. [PubMed: 23298610]

38. Cheng A, Hardingham TE, Kimber SJ. Generating cartilage repair from pluripotent stem cells. Tissue Eng Part B. 2014;20:257–266. 10.1089/ten.teb.2012.0757.

39. Badileanu A, Mora-Navarro C, Martins AMG, et al. Fast automated approach for the derivation of acellular extracellular matrix scaffolds from porcine soft tissues. ACS Biomater Sci Eng. 2020;6:4200–4213. 10.1021/acsbiomaterials.0c00265. [PubMed: 33463339]

40. Crapo PM, Gilbert TW, Badylak SF. An overview of tissue and whole organ decellularization processes. Biomaterials. 2011;32:3233–3243. 10.1016/j.biomaterials.2011.01.057. [PubMed: 21296410]

41. Francesco DD, Varsavia CD, Casarella S, et al. Characterisation of matrix-bound nanovesicles (MBVs) isolated from decellularised bovine pericardium: new frontiers in regenerative medicine. Int J Mol Sci. 2024;25:740. 10.3390/ijms25020740. [PubMed: 38255814]

42. Momenbeitollahi N, Aggarwal R, Strohle G, Bouriayee A, Li H. Extracellular vesicle (EV) dot blotting for multiplexed EV protein detection in complex biofluids. Anal Chem. 2022;94:7368–7374. 10.1021/acs.analchem.2c00846. [PubMed: 35533397]

43. Surti PV, Kim MW, Phan LMT, et al. Progress on dot-blot assay as a promising analytical tool: detection from molecules to cells. TrAC, Trends Anal Chem. 2022;157, 116736. 10.1016/j.trac.2022.116736.

44. Kumar MA, Baba SK, Sadida HQ, et al. Extracellular vesicles as tools and targets in therapy for diseases. Signal Transduct Targeted Ther. 2024;9:27. 10.1038/s41392-024-01735-1.

45. Jiang L, Nelson GW, Abda J, Foord JS. Novel modifications to carbon-based electrodes to improve the electrochemical detection of dopamine. ACS Appl Mater Interfaces. 2016;8:28338–28348. 10.1021/acsami.6b03879. [PubMed: 27420730]

46. Frutiger A, Tanno A, Hwu S, Tiefenauer RF, Voros J, Nakatsuka N. Nonspecific Binding Fundamental concepts and consequences for biosensing applications. Chem. Rev. 2021;121:8095–8160. 10.1021/acs.chemrev.1c00044. [PubMed: 34105942]

47. Lazanas ACh Prodromidis MI. Electrochemical impedance Spectroscopy A tutorial. ACS Meas. Sci. Au. 2023;3:162–193. 10.1021/acsmeasuresciau.2c00070. [PubMed: 37360038]

48. Kuphal M, Mills CA, Korri-Youssoufi H, Samitier J. Polymer-based technology platform for robust electrochemical sensing using gold microelectrodes. Sensor Actuator B Chem. 2012;161:279–284. 10.1016/j.snb.2011.10.032.

49. Liustrovaite V, Drobysh M, Rucinskiene A, et al. Towards an electrochemical immunosensor for the detection of antibodies against SARS-CoV-2 spike protein. J Electrochem Soc. 2022;169, 037523. 10.1149/1945-7111/ac5d91.

50. Leva-Bueno J, Peyman SA, Millner PA. A review on impedimetric immunosensors for pathogen and biomarker detection. Med Microbiol Immunol. 2020;209:343–362. 10.1007/s00430-020-00668-0. [PubMed: 32246198]

51. Cimafonte M, Fulgione A, Gaglione R, et al. Screen printed based impedimetric immunosensor for rapid detection of Escherichia coli in drinking water. Sensors. 2020;20:274. 10.3390/s20010274. [PubMed: 31947810]

52. Sharma S, Rasool HI, Palanisamy V, et al. Structural-mechanical characterization of nanoparticle exosomes in human saliva, using correlative AFM, FESEM, and force spectroscopy. ACS Nano. 2010;4:1921–1926. 10.1021/nn901824n. [PubMed: 20218655]

53. Li X, Yu Y, Wei R, et al. In vitro and in vivo study on angiogenesis of porcine induced pluripotent stem cell-derived endothelial cells. Differentiation. 2021;120:10–18. 10.1016/j.diff.2021.05.003. [PubMed: 34116291]

54. Izadpanah M, Bakhshayesh ARD, Bahroudi Z, et al. Melatonin and endothelial cell-loaded alginate-fibrin hydrogel promoted angiogenesis in rat cryopreserved/thawed ovaries transplanted to the heterotopic sites. J Biol Eng. 2023;17:23. 10.1186/s13036-023-00343-x. [PubMed: 36978096]

55. Pellegata AF, Dominioni T, Ballo F, et al. Arterial decellularized scaffolds produced using an innovative automatic system. Cells Tissues Organs. 2015;200:363–373. 10.1159/000439082. [PubMed: 26562773]

56. nal MS, Darcan C, Akpek A. Characterization of a decellularized sheep pulmonary heart valves and analysis of their capability as a xenograft initial matrix material in heart valve tissue engineering. Bioengineering. 2023;10:949. 10.3390/bioengineering10080949. [PubMed: 37627834]

57. Hamilton AG, Townsend JM, Detamore MS. Automated decellularization of musculoskeletal tissues with high extracellular matrix retention. Tissue Eng C Methods. 2022;28:137–147. 10.1089/ten.tec.2022.0005.

58. Gilbert TW, Sellaro TL, Badylak SF. Decellularization of tissues and organs. Biomaterials. 2006;27:3675–3683. 10.1016/j.biomaterials.2006.02.014. [PubMed: 16519932]

59. Hong P, Bezuhly M, Graham ME, Gratzer PF. Efficient decellularization of rabbit trachea to generate a tissue engineering scaffold biomatrix. Int J Pediatr Otorhinolaryngol. 2018;112:67–74. 10.1016/j.ijporl.2018.06.032. [PubMed: 30055743]

60. Guimaraes AB, Correia AT, Alves BP, et al. Evaluation of a physical-chemical protocol for porcine tracheal decellularization. Transplant. 2019;P 51:1611–1613. 10.1016/j.transproceed.2019.01.042.

61. Crum RJ, Hall K, Molina CP, et al. Immunomodulatory matrix-bound nanovesicles mitigate acute and chronic pristane-induced rheumatoid arthritis. Npj Regen Medicine. 2022;7:13. 10.1038/s41536-022-00208-9.

62. Shapiro IM, Landis WJ, Risbud MV. Matrix vesicles: are they anchored exosomes? Bone. 2015;79:29–36. 10.1016/j.bone.2015.05.013. [PubMed: 25980744]

63. Rogers MA, Buffolo F, Schlotter F, et al. Annexin A1–dependent tethering promotes extracellular vesicle aggregation revealed with single–extracellular vesicle analysis. Sci Adv. 2020;6. 10.1126/sciadv.abb1244.eabb1244.

64. Linares R, Tan S, Gounou C, Arraud N, Brisson AR. High-speed centrifugation induces aggregation of extracellular vesicles. J Extracell Vesicles. 2015;4, 29509. 10.3402/jev.v4.29509. [PubMed: 26700615]

65. Takahashi Y, Takakura Y. Extracellular vesicle-based therapeutics: extracellular vesicles as therapeutic targets and agents. Pharmacol Ther. 2023;242, 108352. 10.1016/j.pharmthera.2023.108352. [PubMed: 36702209]

66. Giannotta M, Trani M, Dejana E. VE-cadherin and endothelial adherens junctions: active guardians of vascular integrity. Dev Cell. 2013;26:441–454. 10.1016/j.devcel.2013.08.020. [PubMed: 24044891]

67. Symon A, Harley V. SOX9: a genomic view of tissue specific expression and action. Int J Biochem Cell Biol. 2017;87:18–22. 10.1016/j.biocel.2017.03.005. [PubMed: 28323209]

68. Choi SH, Lee K, Han H, et al. Prochondrogenic effect of decellularized extracellular matrix secreted from human induced pluripotent stem cell-derived chondrocytes. Acta Biomater. 2023. 10.1016/j.actbio.2023.05.052.

69. Faleeva M, Ahmad S, Theofilatos K, et al. Sox9 accelerates vascular aging by regulating extracellular matrix composition and stiffness. Circ Res. 2024;134:307–324. 10.1161/circresaha.123.323365. [PubMed: 38179698]

70. Chinnadayyala SR, Cho S. Electrochemical immunosensor for the early detection of rheumatoid arthritis biomarker: anti-cyclic citrullinated peptide antibody in human serum based on avidin-biotin system. Sensors. 2020;21:124. 10.3390/s21010124. [PubMed: 33379138]

71. Kilic T, Cho YK, Jeong N, et al. Multielectrode spectroscopy enables rapid and sensitive molecular profiling of extracellular vesicles. ACS Cent Sci. 2022;8:110–117. 10.1021/acscentsci.1c01193. [PubMed: 35111901]

72. Lee S, Crulhas BP, Suvakov S, et al. Nanoparticle-enabled multiplexed electrochemical immunoassay for detection of surface proteins on extracellular vesicles. Acs Appl Mater Inter. 2021;13:52321–52332. 10.1021/acsami.1c14506.

73. Sebaihi N, Boeck BD, Yuana Y, Nieuwland R, Pétry J. Dimensional characterization of extracellular vesicles using atomic force microscopy. Meas Sci Technol. 2017;28,034006. 10.1088/1361-6501/28/3/034006.
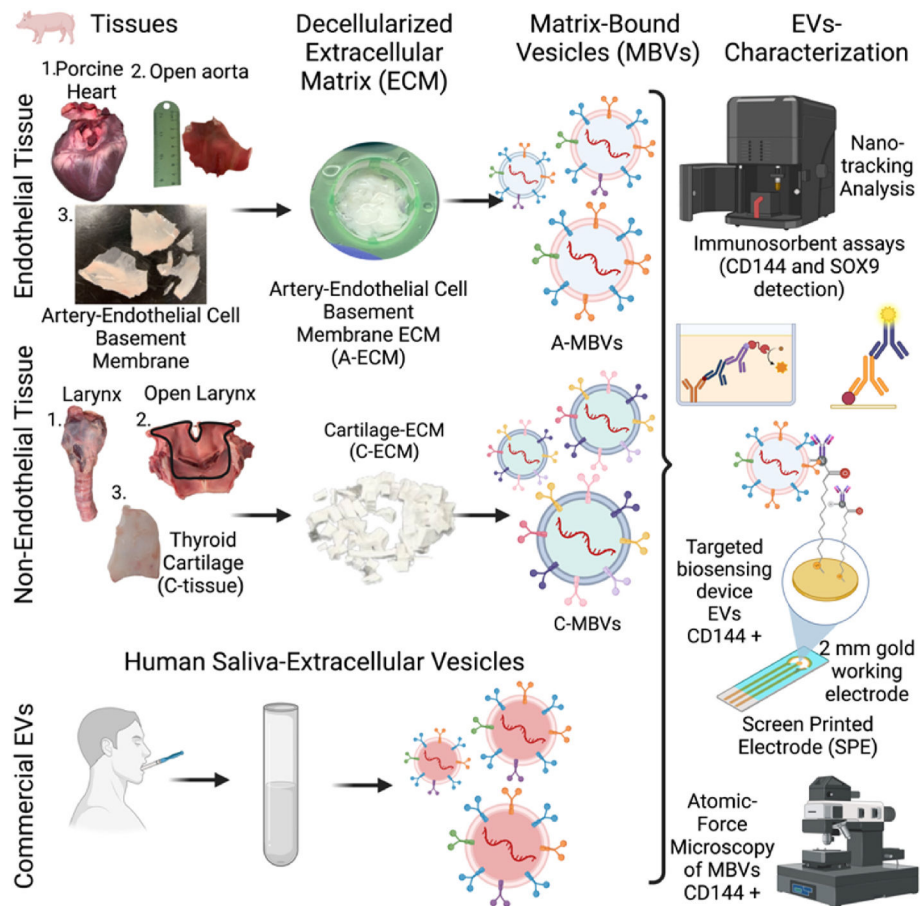
Fig. 1.

Overview. Two porcine tissues, endothelial cell basement membrane from arteries and thyroid cartilage, were decellularized to isolate their respective Matrix-Bound Vesicles (MBVs)—A-MBVs and C-MBVs. Commercial extracellular vesicles from healthy individual saliva were used as controls. Characterization revealed CD144 predominantly in endothelial EVs, supporting its use as an endothelial biomarker, whereas SOX9 was identified in C-MBVs associated with chondrocytes. Immunodetection techniques facilitated the development of a prototype biosensor for MBV biomarker detection, with AFM used to characterize MBVs on the immunofunctionalized gold surface. Created with BioRender.com.
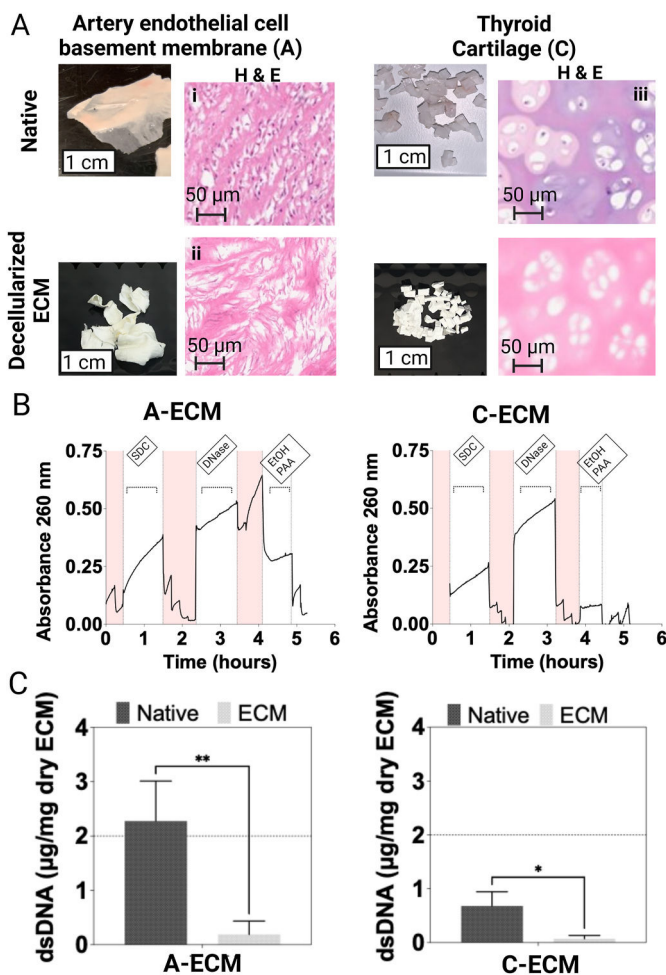
Fig. 2.

Characterization of Native and dECM. **A.** Overview of Tissue Samples: Macro views from left to right; the top panel shows native tissues of Endothelial Cell Basement Membrane from Artery (A) and Thyroid Cartilage (C), and the bottom panel displays corresponding dECM.i-iv H&E staining for microview evaluation. **B.** Decellularization Monitoring Curves: Displays for A-ECM and C-ECM. The X-axis represents time in hours, and the Y-axis shows absorbance at 260 nm. Highlighted sections indicate washing steps involving DI water, DPBS, and DI water, with treatment agents including SDC, DNase Type II, and EtOH with 0.1% v/v peracetic acid. **C.** dsDNA Quantification: Comparison of dsDNA levels from left to right for A-ECM and C-ECM with dark bars representing native tissue and light bars representing dECM. Created with BioRender.com.
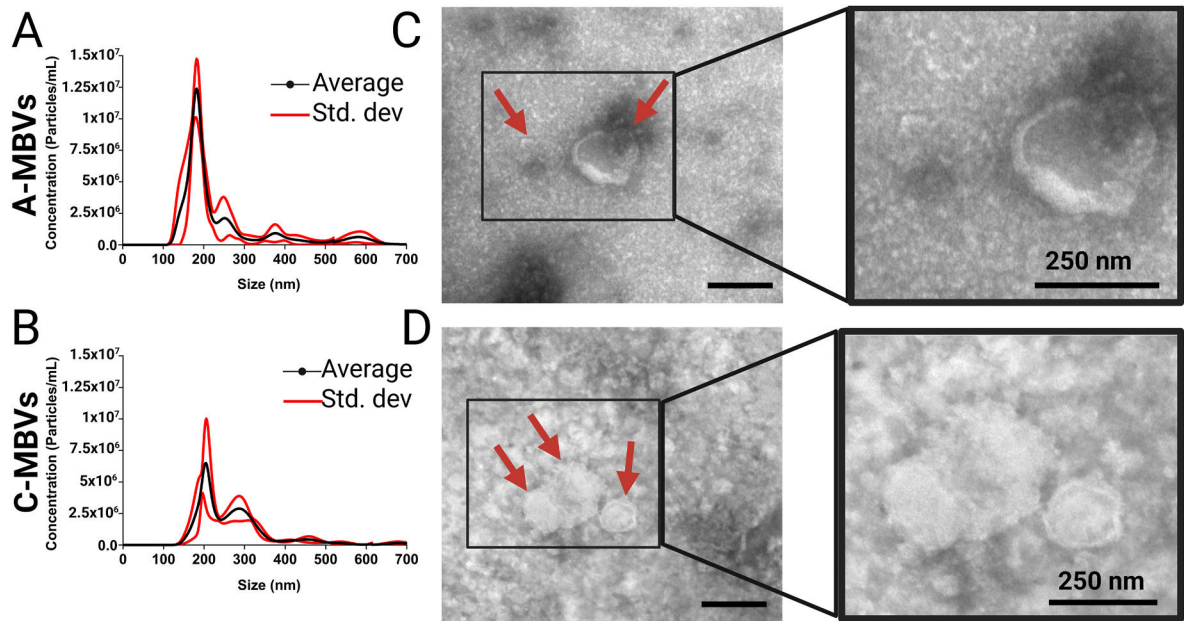
Fig. 3.

Characterization of Isolated MBVs. Nanoparticle Tracking Analysis (NTA) shows the size distribution of (A) A-MBVs and (B) C-MBVs along the X-axis with particle size (nm) and Y-axis displaying concentration as particles/mL. The red lines indicate the standard deviation, and the black line represents the average based on at least three replicates. Inset images from Transmission Electron Microscopy (TEM) highlight (C) A-MBVs and (D) C-MBVs with red arrows pointing to the EVs. Scale bar = 250 nm. Created with BioRender.com.
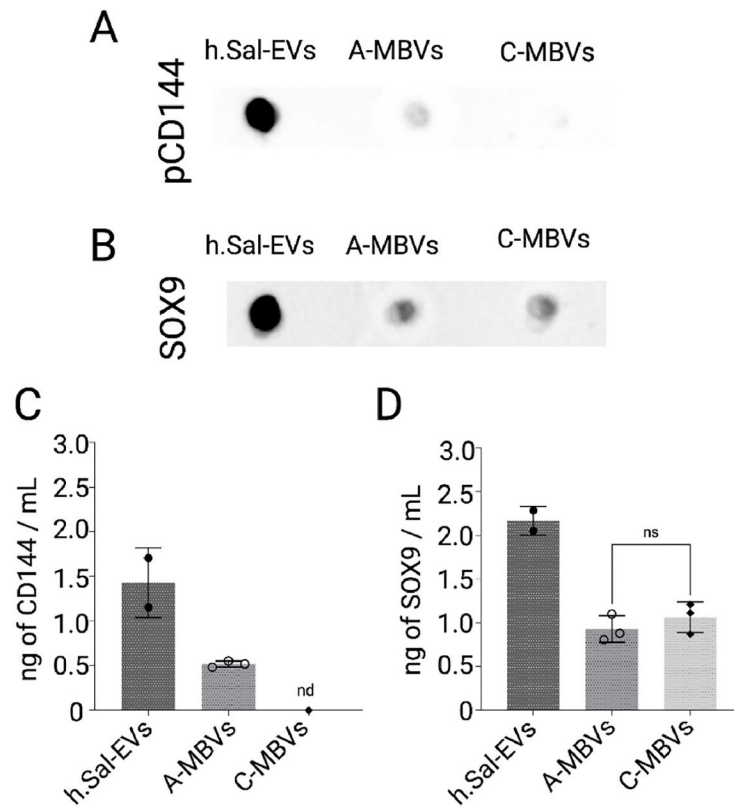
Fig. 4.
Immunoblotting assays and quantification of targeted proteins in extracellular vesicles. **A:** Detection of porcine VE-cadherin (CD144) in human saliva EVs (h.Sal-EVs), artery-derived MBVs (A-MBVs), and cartilage-derived MBVs (C-MBVs). **B:** Detection of SRY-related high-mobility-group box 9 (SOX9) in h.Sal-EVs, A-MBVs, and C-MBVs. **C:** Enzyme-linked immunosorbent assay (ELISA) quantification of CD144 in h.Sal-EVs, A-MBVs, and C-MBVs. D: ELISA quantification of SOX9 in h.Sal-EVs, A-MBVs, and C-MBVs. nd = no detected. Created with BioRender.com.
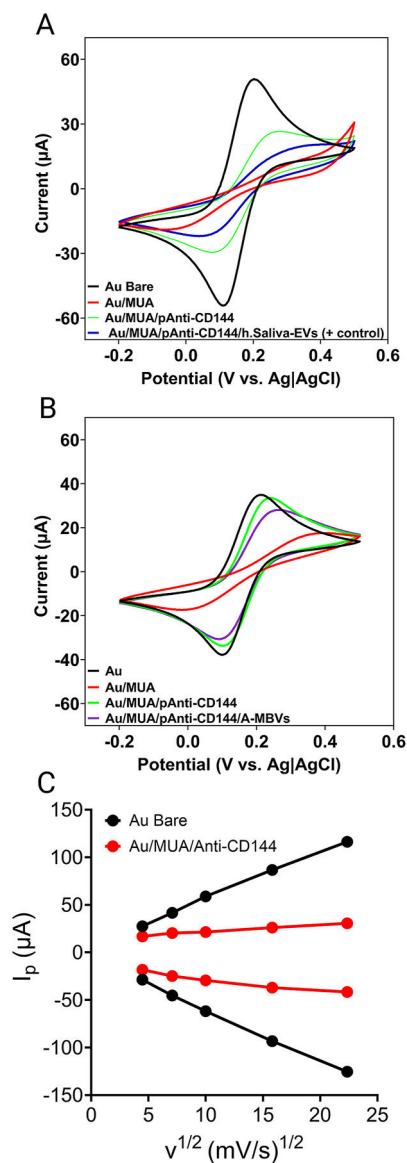
Fig. 5.
Cyclic voltammetry of **A**, Au Bare, Au/MUA, Au/MUA/anti-CD144 and Au/MUA/anti-CD144/human Saliva EVs (h.Sal-EVs). **B**, Au Bare, Au/MUA, Au/MUA/anti-CD144 and Au/MUA/anti-CD144/A-MVBs. All cyclic voltammetry experiments were done in a 5 mM K_3FeCN_6/K_4FeCN_6 solution in 0.1 M KCl. C, Intensity peak (Ip) vs square root of scan rate $(v^{1/2})$.
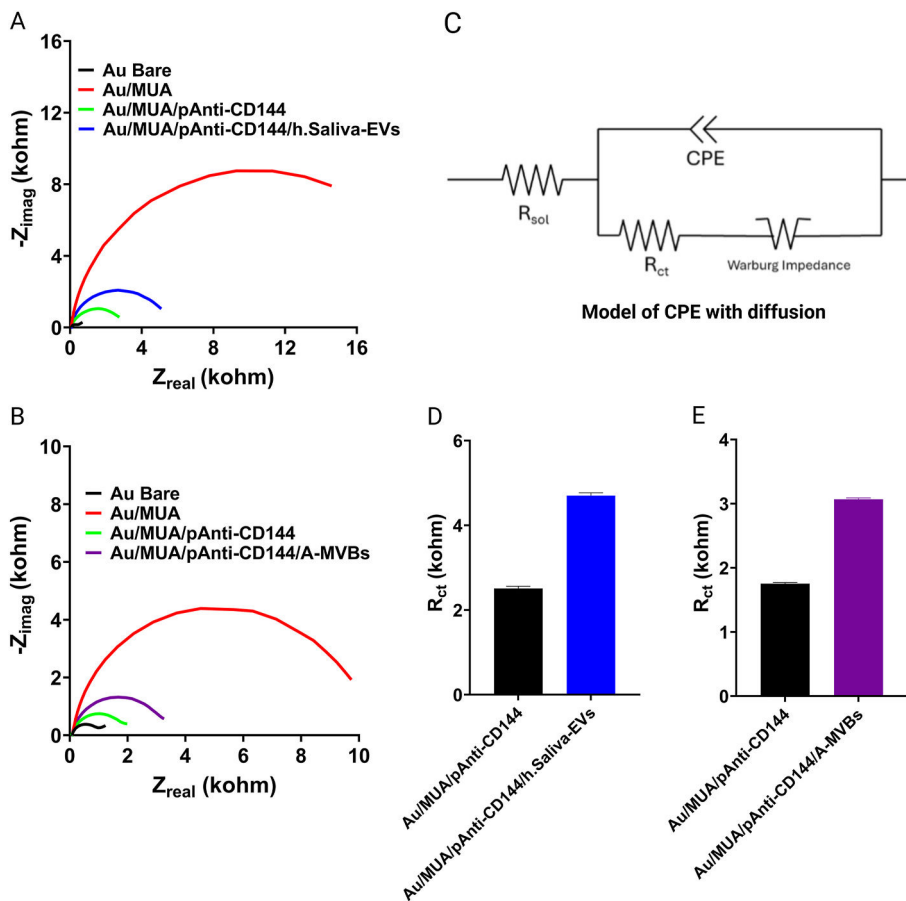
Fig. 6.
Electrochemical characterization of functionalized SPEs and detection of isolated MBVs, Nyquist Plot of the detection of, **A**. human Saliva Extracellular Vesicles (h.Saliva-EVs), **B**. Artery Matrix-Bound Vesicles (A-MBVs), and **C.** Equivalent circuit of Nyquist Plot. Resistance to charge transfer plot of functionalization steps, **D.** Detection of h. Saliva-EVs, and **E.** Detection of A-MBVs.
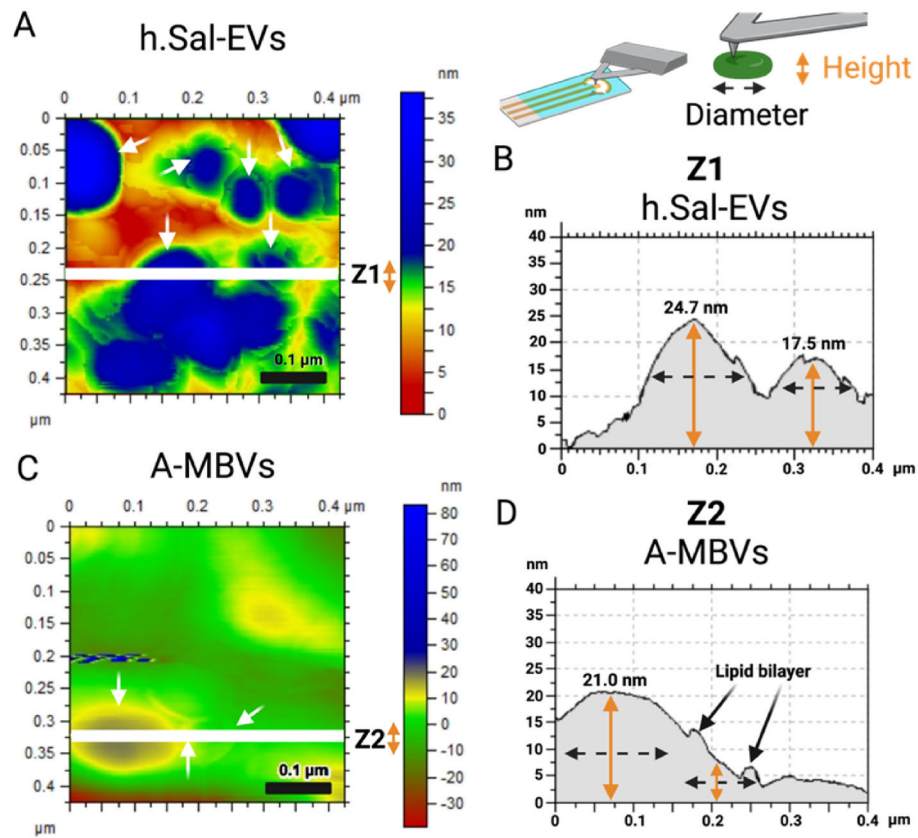
Fig. 7.
Atomic Force Microscopy (AFM) images showing **A:** the topography of human saliva extracellular vesicles (h.Sal-EVs) with white arrows indicating EVs; **B:** diameter (black arrows) and height (gold arrows) analyses in Zone 1 (Z1); **C:** the topography of artery matrix-bound vesicles (A-MBVs) with white arrows pointing to isolated MBVs; and **D:** diameter (black arrows) and height (gold arrows) analyses in Zone 2 (Z2). Created with BioRender.com.

Table 1

Summary of dECM production protocol.

Decellularization steps	Time (minutes)
DI water	10
1X DPBS	10
DI water	10
SDC (4%)	60
DI water	10
1X DPBS	10
DI water	10
DNase (1 mg/mL)	60
DI water	10
1X DPBS	10
DI water	10
4% EtOH and 0.1% PAA	30–60
DI water	10
1X DPBS	10
DI water	10

EtOH: Ethanol and PAA: Peracetic acid.